JOURNAL OF GUIDANCE, CONTROL, AND DYNAMICS
Vol. 24, No. 6, November–December 2001

Nonlinear Flight Control Using Forebody Tangential Blowing

Yuji Takahara* and Stephen M. Rock†
Stanford University, Stanford, California 94305-4035

A novel nonlinear approach is presented to designing aircraft control laws based on combining high-gain control and Lyapunov techniques. The approach is applied and demonstrated experimentally to control the lateral-directional dynamics of an aircraft at high angle of attack using forebody tangential blowing (FTB). FTB is a pneumatic device that modifies the vortical flow over the forebody. The modified vortical flow in turn creates roll and yaw moments for control characterized by highly nonlinear and uncertain input/output characteristics. The control approach presented here robustly inverts these characteristics and enables the exploitation of the full FTB efficiency. The control approach is applicable in general to nonlinear systems which are actuated by a subsystem comprising uncertain static nonlinearities and linear dynamics.

Nomenclature

$C(\boldsymbol{q}, \dot{\boldsymbol{q}})$	=	generalized damping matrix
C_f	=	friction coefficient matrix
C_l	=	roll moment coefficient
C_n	=	yaw moment coefficient
C_μ	=	jet moment coefficient
c	=	scalar constant
c_{fi}	=	friction coefficient
F_{a_0}, F_a	=	system matrix (aerodynamic system)
$f(\boldsymbol{x})$	=	nonlinear system function (rigid body)
G_{a_0}, G_a	=	input matrix (aerodynamic system)
$g(\boldsymbol{x})$	=	nonlinear input function (rigid body)
$H(\boldsymbol{q})$	=	generalized inertia matrix
H_{a_0}, H_a	=	output matrix (aerodynamic system)
I	=	identity matrix
I_A	=	moment of inertia of apparatus
I_x, I_y, I_z	=	moment of inertia of model x, y, z axis
I_{xz}	=	product of inertia of model y axis
K_d	=	derivative gain matrix
K_i	=	integral gain matrix
K_p	=	proportional gain matrix
$k(\boldsymbol{x})$	=	virtual control for rigid body
k_{δ_f}	=	flaperon effectiveness coefficient
$\boldsymbol{m}$	=	aerodynamic moment
m_f	=	friction moment
m_g	=	gravity torque
m_m	=	motor torque
$\boldsymbol{m}_s$	=	static aerodynamic moment
m_T	=	total moment
$\boldsymbol{m}_v$	=	virtual moment, $k(x)$
$\dot{m}_j$	=	mass flow rate through the slot
$\bar{\boldsymbol{m}}_s$	=	nominal static aerodynamic moment
$\boldsymbol{q}$	=	generalized coordinates, $[\phi \gamma]^T$
q_∞	=	freestream dynamic pressure
S_{ref}	=	reference area, wing planform area
$\boldsymbol{s}$	=	manifold, $\boldsymbol{m} - k(\boldsymbol{x})$
$\boldsymbol{u}$	=	input, $[C_\mu \ \ \delta_f]^T$
V_j	=	jet exit velocity
$\boldsymbol{V}_s$	=	Lyapunov function for s
V_x	=	Lyapunov function for x
V_∞	=	wind-tunnel speed
$\boldsymbol{x}$	=	rigid-body state, $[\phi \ \ \gamma \ \ \dot{\phi} \ \ \dot{\gamma}]^T$
$\boldsymbol{y}$	=	output, $[\boldsymbol{x}^T \ \ \boldsymbol{m}^T]^T$
$\boldsymbol{\alpha}_s$	=	decay rate of s
γ	=	approximate yaw angle
$\boldsymbol{\delta m}_s$	=	unknown static aerodynamic moment
δ_f	=	flaperon deflection
$\boldsymbol{\eta}$	=	aerodynamic states
$\hat{\boldsymbol{\eta}}$	=	estimate of aerodynamic states
$\tilde{\boldsymbol{\eta}}$	=	estimation error, $\eta - \hat{\eta}$
$\boldsymbol{\kappa}$	=	high-gain parameter
$\tilde{\boldsymbol{\kappa}}$	=	modified high-gain parameter
λ	=	eigenvalue
ρ	=	upper bound of δm_s
$\tilde{\rho}$	=	modified upper bound of uncertainties
τ	=	time constant
ϕ	=	roll angle

I. Introduction

FOREBODY tangential blowing (FTB) has been shown to be a very powerful means of generating forces and moments on aircraft operating in flight regimes where the effectiveness of conventional aerodynamic surfaces is reduced, for example, high angle of attack, poststall.[1,2] Consequently, it provides a mechanism that could greatly expand the flight envelope of future aircraft systems. Furthermore, it offers a means of generating forces and moments that could replace conventional surfaces in other regions of the operating envelope.

One major factor that currently limits the use of FTB is that it is highly nonlinear and uncertain where it is most efficient. That is, FTB provides very powerful effects, for example, forces and moments, at low levels of blowing, but the characteristic relating input to output is very nonlinear in this region. On the other hand, if higher levels of blowing are used, then the characteristics become well behaved, but the control effort increases. Hence, the trade between robustness and control usage is particularly acute. To exploit the high efficiency possible with FTB, a new approach must be developed. The ultimate goal of this work, therefore, is to develop a new generic approach to nonlinear control design that can robustly exploit the efficiency of powerful but highly nonlinear and uncertain systems. With such an approach, FTB can be a very efficient device for flight control at high angles of attack.

Previous studies have shown that control laws using FTB can be developed using conventional nonlinear control approaches.[3,4] These studies successfully demonstrated that significant improvement in high-angle-of-attack performance could be achieved using FTB. However, the approaches avoid much of the nonlinear nature of the device and result in excessive use of blowing air to achieve the control power. As already mentioned, to exploit the full efficiency possible with FTB, a controller must operate at low levels of blowing, where the actuation effects are highly nonlinear. This objective could be achieved with a control law that could invert the nonlinear characteristics. However, the inversion of highly nonlinear

Received 15 May 2000; revision received 8 February 2001; accepted for publication 29 March 2001.

*Research Assistant, Department of Aeronautics and Astronautics; currently Deputy Director, Research and Development Planning Division, Bureau of Finance and Equipment, Japan Defense Agency, Tokyo, Japan; takahara@tkf.att.me.jp.

†Associate Professor, Department of Aeronautics and Astronautics; rock@sun-valley.stanford.edu. Senior Member AIAA.

characteristics that involve a high degree of uncertainty can lead to a very sensitive, and possibly unstable, closed-loop system. Consequently, any such inversion technique must be robust and explicitly take into account the associated uncertainties. Only in this way can satisfactory performance be guaranteed.

This paper presents an approach to nonlinear control based on combining high-gain control (HGC)[5,6] and Lyapunov techniques.[7,8] It is generically applicable to nonlinear systems that are actuated by a subsystem comprising uncertain static nonlinearities and linear dynamics. The approach consists of a few simple steps that allow time-scale separation of each step. Neither upper bounds on the uncertainties nor a full-dimensional Lyapunov function is required. It allows explicit tradeoff between the performance and the control effort.

The experimental apparatus used in this study is presented in Sec. II, and the mathematical model of the FTB system is described in Sec. III. The details of the approach are described in Sec. IV. In Sec. V, this design is applied to two-degrees-of-freedom(DOF) set-point tracking problems, and experimental results are presented. An appendix containing proofs of key mathematical steps is included at the end.

II. Experimental Apparatus

The system consists of a tailless, delta wing model inside a small wind tunnel located at Stanford University (Fig. 1). The length of the model is 11 in. and the wing span is 5.8 in. A unique support system[9] is used that constrains the model to two DOF. The objective is to approximate the lateral–directional dynamics of an aircraft. The model is free to roll (ϕ) about its longitudinal axis and to rotate about an axis fixed in space and passing through the body as shown in Fig. 1 (this rotation angle is γ and will be referred to as yaw). The nominal incidence is fixed at 45 deg. This model has both an FTB system and movable flaperons as control effector (Fig. 2). Blowing slots exist along both sides of the model's forebody through which air can be injected tangent to the body surface. Air is blown through only one slot at a time to minimize total air usage. C_μ is the jet moment coefficient defined as

$$C_\mu = \frac{\dot{m}_j V_j}{q_\infty S_{\text{ref}}}$$

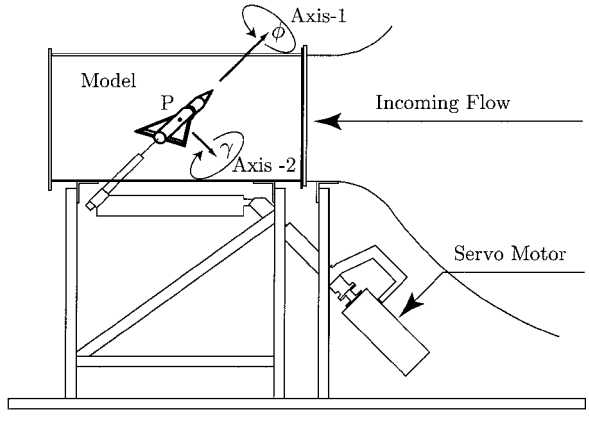

Fig. 1 Schematic of wind-tunnel experimental apparatus.

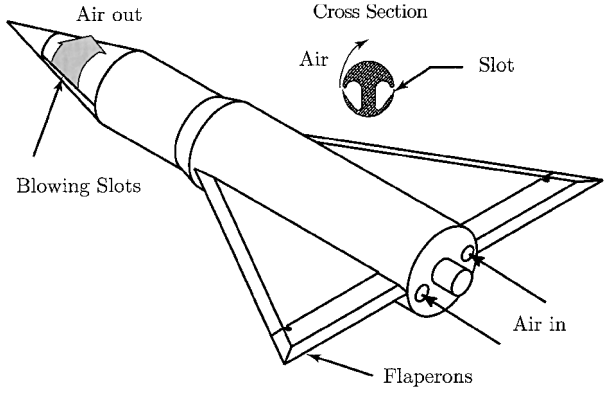

Fig. 2 Wind-tunnel model and detail of forebody slots.

Movable flaperons attached to the trailing edges can be controlled independently. In this research, however, they are used differentially, that is, they are always deflected by the same amount in the opposite direction. Here δ_f is the flaperon deflection.

III. FTB System Model

A mathematical model of the FTB system describes the rigid-body dynamics and the aerodynamics. The key element of the FTB system model is the aerodynamics. Aerodynamics at high angles of attack is very complicated due to separated flow, vortex shedding, and possibly vortex breakdown. In this research, the model of aerodynamic effects is based on the work by Pedreiro[9] in which it was shown that the aerodynamic moments can be well modeled using lagged static loads. This approach is simple enough for the use of control design but captures all of the important aspects of the aerodynamics.

A. Rigid-Body Dynamics

The equations of motion of the rigid-body aircraft expressed in terms of two DOF, ϕ and γ, for large angles are developed in Ref. 9. They are

$$I_x\ddot{\phi} + I_{xz}\ddot{\gamma}\cos\phi + (I_z - I_y)\dot{\gamma}^2\sin\phi\cos\phi = m_{T1} \tag{1}$$

$$\left(I_A + I_y\sin^2\phi + I_z\cos^2\phi\right)\ddot{\gamma} + I_{xz}(\ddot{\phi}\cos\phi - \dot{\phi}^2\sin\phi) + 2(I_y - I_z)\dot{\phi}\dot{\gamma}\sin\phi\cos\phi = m_{T2} \tag{2}$$

where I_* are the inertia properties about the point P and m_* are moments. The suffixes are x, y, z for the body-fixed orthonormal frame, 1 for the roll axis (body-fixed x axis), 2 for the yaw shaft axis (inertia frame), A for the apparatus and T for total. The physical parameters are

$$I_x = 3.5620 \times 10^{-4}\ (\text{kg m}^2), \qquad I_y = 3.7067 \times 10^{-3}\ (\text{kg m}^2)$$

$$I_z = 3.9531 \times 10^{-3}\ (\text{kg m}^2), \qquad I_{xz} = 0.0\ (\text{kg m}^2)$$

$$I_A = 0.1772\ (\text{kg m}^2)$$

In the preceding equations, m_T can be decomposed as

$$m_{T1} = m_1 + m_{f1}, \qquad m_{T2} = m_2 + m_{f2} + m_g + m_m \tag{3}$$

where m_1 and m_2 are the aerodynamic moments and the other subscripts indicate the origin of additional moments: friction of bearings and potentiometer f, gravity restoring moment g, and motor m.

Incorporating an active torque cancelation (ATC) developed in Ref. 9 yields torque applied by the motor equal to

$$m_m = -m_g + 0.9I_A\ddot{\gamma} \tag{4}$$

The purpose of ATC is to eliminate the effect of the gravity torque and reduce the effect of the large moment of inertia of the apparatus (90% reduction[10]) so that the motion of the aircraft model is dominated by aerodynamic loads. Finally, the moments due to friction of the bearings and potentiometers were measured experimentally and can be written as

$$m_{f1} = -c_{f1}\dot{\phi}, \qquad m_{f2} = -c_{f2}\dot{\gamma} \tag{5}$$

where

$$c_{f1} = 1.54 \times 10^{-3}\ (\text{N}\cdot\text{m/s}), \qquad c_{f2} = 1.10 \times 10^{-2}\ (\text{N}\cdot\text{m/s}) \tag{6}$$

Substituting Eqs. (3–5) into Eqs. (1) and (2) yields the equations of motion as

$$I_x\ddot{\phi} + I_{xz}\ddot{\gamma}\cos\phi + (I_z - I_y)\dot{\gamma}^2\sin\phi\cos\phi = m_1 - c_{f1}\dot{\phi} \tag{7}$$

$$\left(I_y\sin^2\phi + I_z\cos^2\phi + 0.1I_A\right)\ddot{\gamma} + I_{xz}(\ddot{\phi}\cos\phi - \dot{\phi}^2\sin\phi) + 2(I_y - I_z)\dot{\phi}\dot{\gamma}\sin\phi\cos\phi = m_2 - c_{f2}\dot{\gamma} \tag{8}$$

These can be rewritten in Euler–Lagrange form as

$$H(\boldsymbol{q})\ddot{\boldsymbol{q}} + C(\boldsymbol{q}, \dot{\boldsymbol{q}})\dot{\boldsymbol{q}} = \boldsymbol{m} - C_f\dot{\boldsymbol{q}} \tag{9}$$

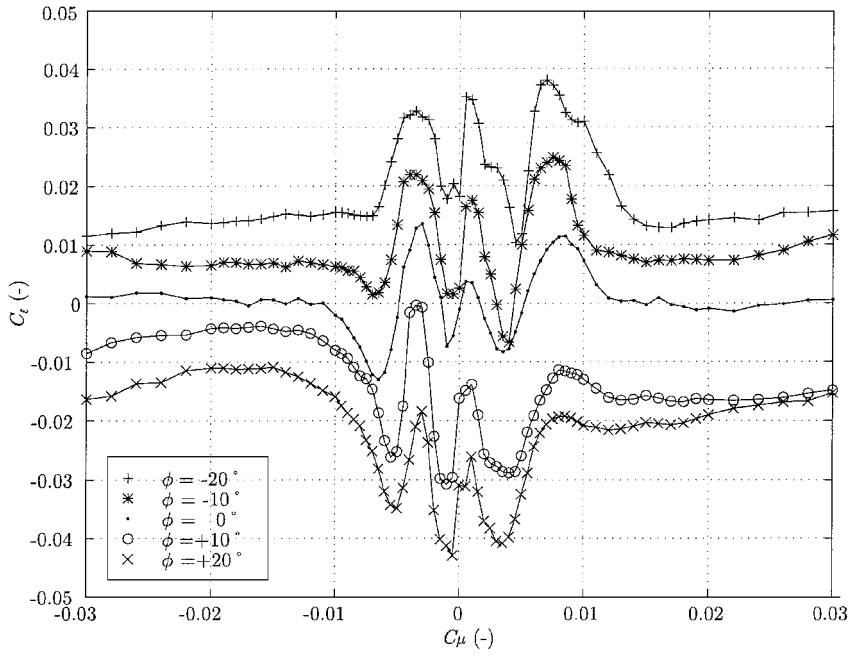

Fig. 3 Roll moment coefficient for various C_μ and ϕ, where $\gamma = \delta_f = 0$.

where

$$\boldsymbol{q} = [\phi \quad \gamma]^T$$

$$H(\boldsymbol{q}) = \begin{bmatrix} I_x & I_{xz}\cos\phi \\ I_{xz}\cos\phi & I_y \sin^2\phi + I_z\cos^2\phi + 0.1 I_A \end{bmatrix}$$

$$C(\boldsymbol{q}, \dot{\boldsymbol{q}}) = \begin{bmatrix} 0 & (I_z - I_y)\dot{\gamma}\sin\phi\cos\phi \\ (I_y - I_z)\dot{\gamma}\sin\phi\cos\phi - I_{xz}\dot{\phi}\sin\phi & (I_y - I_z)\dot{\phi}\sin\phi\cos\phi \end{bmatrix}$$

$$C_f = \begin{bmatrix} c_{f1} & 0 \\ 0 & c_{f2} \end{bmatrix}$$

Finally, these equations can be written in a state-variable form by solving for $\ddot{\phi}$ and $\ddot{\gamma}$:

$$\begin{bmatrix} \boldsymbol{q} \\ \dot{\boldsymbol{q}} \end{bmatrix} = \begin{bmatrix} 0 & I \\ 0 & -H(\boldsymbol{q})^{-1}\tilde{C}(\boldsymbol{q}, \dot{\boldsymbol{q}}) \end{bmatrix} \begin{bmatrix} \boldsymbol{q} \\ \dot{\boldsymbol{q}} \end{bmatrix} + \begin{bmatrix} 0 \\ H(\boldsymbol{q})^{-1} \end{bmatrix} \boldsymbol{m} \tag{10}$$

$$\tilde{C}(\boldsymbol{q}, \dot{\boldsymbol{q}}) = C(\boldsymbol{q}, \dot{\boldsymbol{q}}) + C_f \tag{11}$$

Hence,

$$\dot{\boldsymbol{x}} = f(\boldsymbol{x}) + g(\boldsymbol{x})\boldsymbol{m}, \qquad f(\boldsymbol{0}) = \boldsymbol{0} \tag{12}$$

where $\boldsymbol{x} = [\boldsymbol{q}^T \quad \dot{\boldsymbol{q}}^T]^T = [\phi \quad \gamma \quad \dot{\phi} \quad \dot{\gamma}]^T$ and the vector $\boldsymbol{m}$ is the applied aerodynamic moment in each DOF $\boldsymbol{m} = [m_1 \quad m_2]^T$.

Note that the inertia properties of the model ($I_{xz} = 0$ and $I_y \approx I_z$) make the rigid-body dynamics nearly diagonal [refer to Eq. (9)]. Furthermore, all of the nonlinear terms in Eq. (9) are small due to $I_y \approx I_z$; hence, the rigid-body dynamics are well approximated by two independent linear time-invariant systems: ϕ and γ. (This characteristic is not necessary, but is used for convenience in designing a specific controller in later sections.)

B. Aerodynamic Model

The aerodynamic moments are expressed as

$$\dot{\boldsymbol{\eta}} = F_a\boldsymbol{\eta} + G_a\boldsymbol{m}_s(\boldsymbol{x}, \boldsymbol{u}) \tag{13}$$

$$\boldsymbol{m} = H_a\boldsymbol{\eta} \tag{14}$$

where $\boldsymbol{\eta}$ is the vector of internal states of the aerodynamics, $\boldsymbol{m}$ is the resultant aerodynamic moments, $\boldsymbol{u}$ is the control input ($\boldsymbol{u} = [C_\mu \quad \delta_f]^T$), and $\boldsymbol{m}_s(\boldsymbol{x}, \boldsymbol{u})$ is the vector of static aerodynamic moments, which are highly nonlinear functions of C_μ. The static aerodynamic moments are described in the next section. Because two independent first-order lags for both aerodynamic moments are used,[9] F_a, G_a, and H_a are expressed as

$$F_a = \begin{bmatrix} -1/\tau_1 & 0 \\ 0 & -1/\tau_2 \end{bmatrix}, \qquad G_a = \begin{bmatrix} 1/\tau_1 & 0 \\ 0 & 1/\tau_2 \end{bmatrix}$$

$$H_a = \begin{bmatrix} 1 & 0 \\ 0 & 1 \end{bmatrix} \tag{15}$$

where $\tau_1 = 0.020$ s and $\tau_2 = 0.0183$ s are the time constant of the lags from $\boldsymbol{m}_{s_1}(\boldsymbol{x}, \boldsymbol{u})$ to $\boldsymbol{m}_1$ and $\boldsymbol{m}_{s_2}(\boldsymbol{x}, \boldsymbol{u})$ to $\boldsymbol{m}_2$. The aerodynamic equation can be simplified as

$$\dot{\boldsymbol{m}} = F_a\boldsymbol{m} + G_a\boldsymbol{m}_s(\boldsymbol{x}, \boldsymbol{u}) \tag{16}$$

because with the $H_a = I$, $\boldsymbol{\eta} \equiv \boldsymbol{m}$.

1. Static Moment

Figures 3 and 4 show typical static moment characteristics [$\boldsymbol{m}_s(\boldsymbol{x}, \boldsymbol{u})$] due to FTB. Roll moment coefficient C_l and yaw moment coefficient C_n are plotted for various C_μ and ϕ at $\gamma = 0, \delta_f = 0$ ($V_\infty = 24.5$ m/s). Figures 3 and 4 show that FTB is most efficient but highly nonlinear at small levels of blowing, whereas it is well behaved at large levels of blowing.

Figures 5 and 6 show the effects of the flaperons[11] on the roll moment C_l and the yaw moment C_n for various C_μ at $\phi = 0$ and $\gamma = 0$. From these data, it is observed that the flaperons are more effective in generating the roll moment than FTB and that they have a small effect on the yaw moment.

2. Model Uncertainties

For the system dealt with here, the rigid-body dynamic properties are easily measured and are, hence, treated as known. The principal source of uncertainty in the system is the aerodynamic model. In particular, the static moment characteristics are the dominant uncertain factors. These uncertainties arise from the errors associated with measuring experimentally the static moments, the blowing coefficient C_μ, and the airspeed.

Given this, the static moment $\boldsymbol{m}_s(\boldsymbol{x}, \boldsymbol{u})$, which is a function of the rigid-body states x and the input ($\boldsymbol{u} = [C_\mu \quad \delta_f]^T$) can be decomposed as follows:

$$\boldsymbol{m}_s(\boldsymbol{x}, \boldsymbol{u}) = \bar{\boldsymbol{m}}_s(\boldsymbol{x}, \boldsymbol{u}) + \delta\boldsymbol{m}_s(\boldsymbol{x}, \boldsymbol{u}) \tag{17}$$

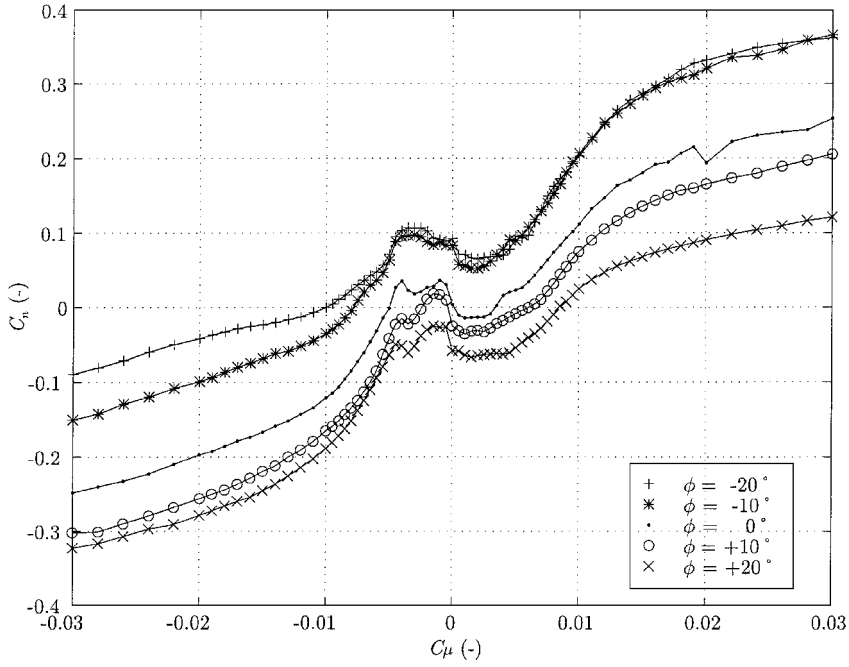

Fig. 4 Yaw moment coefficient for various C_μ and ϕ, where $\gamma = \delta_f = 0$.

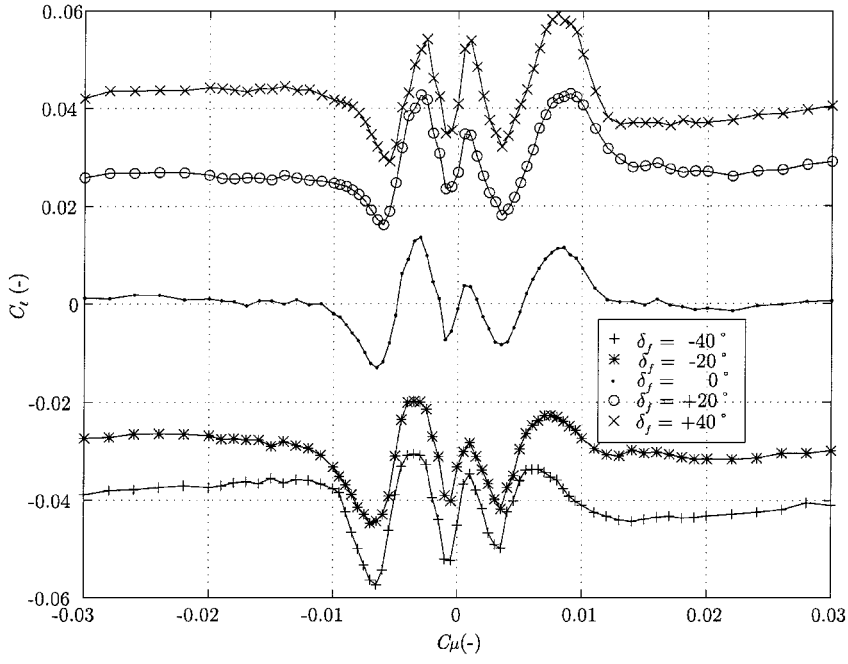

Fig. 5 Flaperon effect on m_{s_1}, where $\phi = \gamma = 0$.

where $\bar{\boldsymbol{m}}_s(\boldsymbol{x}, \boldsymbol{u})$ is the vector of known nominal static aerodynamic moments given in numerical data and $\boldsymbol{\delta m}_s(\boldsymbol{x}, \boldsymbol{u})$ is the vector of uncertain static aerodynamic moments. Schematically, the uncertain static moment is shown in Fig. 7.

Note that the constants τ_1 and τ_2 in the aerodynamic model can also be uncertain. Hence, Eq. (16) can be expressed in the following form:

$$\dot{\boldsymbol{m}} = (F_a + \delta F_a)\boldsymbol{m} + (G_a + \delta G_a)[\bar{\boldsymbol{m}}_s(\boldsymbol{x}, \boldsymbol{u}) + \boldsymbol{\delta m}_s(\boldsymbol{x}, \boldsymbol{u})] \quad (18)$$

If all of the system uncertainties are lumped into w defined as

$$\boldsymbol{w} = G_a^{-1}[\delta F_a \boldsymbol{m} + G_a \boldsymbol{\delta m}_s(\boldsymbol{x}, \boldsymbol{u}) + \delta G_a \bar{\boldsymbol{m}}_s(\boldsymbol{x}, \boldsymbol{u}) + \delta G_a \boldsymbol{\delta m}_s(\boldsymbol{x}, \boldsymbol{u})] \quad (19)$$

the resulting equation becomes

$$\dot{\boldsymbol{m}} = F_a \boldsymbol{m} + G_a[\bar{\boldsymbol{m}}_s(\boldsymbol{x}, \boldsymbol{u}) + \boldsymbol{w}] \quad (20)$$

Note that each component of w is not necessarily small, but it is assumed bounded by an unknown constant, that is,

$$|w_i| \leq \rho_i(\text{unknown}), \qquad (i = 1, 2) \quad (21)$$

3. Nominal Static Aerodynamic Moment

The nominal aerodynamic moments $\bar{\boldsymbol{m}}_{s_1}$ (roll) and $\bar{\boldsymbol{m}}_{s_2}$ (yaw) are found experimentally to be well represented by

$$\bar{\boldsymbol{m}}_{s_1}(\boldsymbol{x}, \boldsymbol{u}) = \bar{\boldsymbol{m}}_{s_1}(\boldsymbol{x}, C_\mu, \delta_f) = \bar{\boldsymbol{m}}_{s_1}(\boldsymbol{x}, C_\mu) + k_{\delta_f}\delta_f \quad (22)$$

$$\bar{\boldsymbol{m}}_{s_2}(\boldsymbol{x}, \boldsymbol{u}) = \bar{\boldsymbol{m}}_{s_2}(\boldsymbol{x}, C_\mu) \quad (23)$$

where

$$k_{\delta_f} = 2.65 \times 10^{-4}\ (\text{N} \cdot \text{m/deg})$$

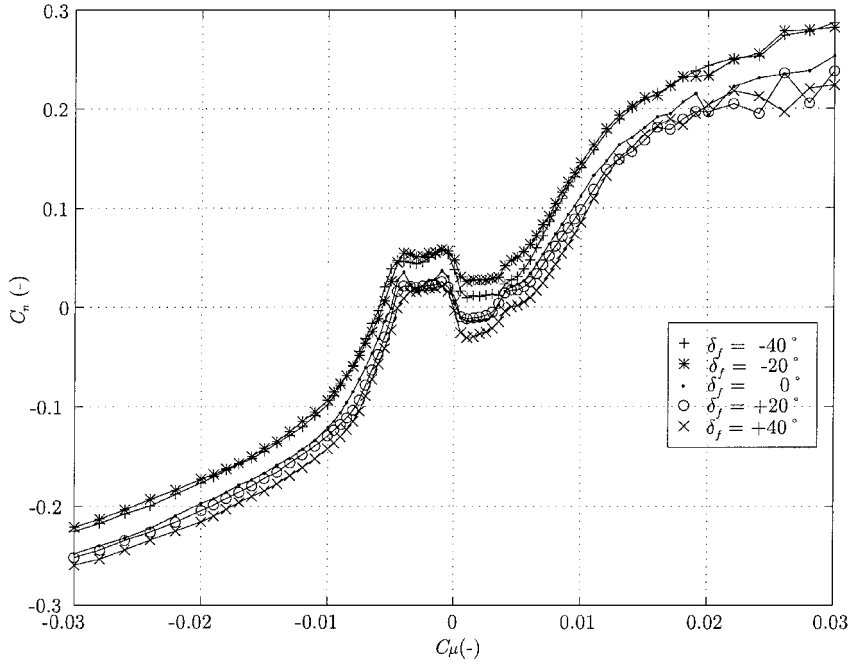

Fig. 6 Flaperon effect on m_{s_2}, where $\phi = \gamma = 0$.

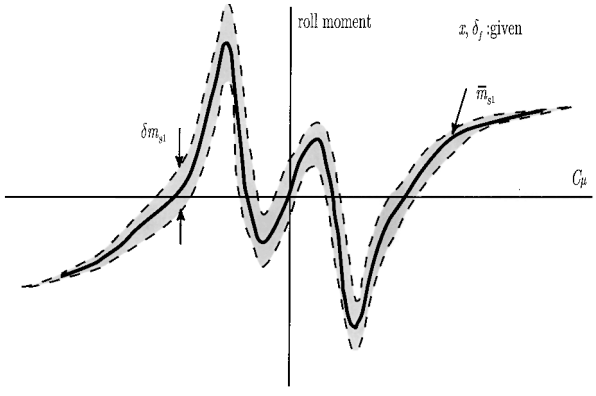

Fig. 7 Uncertain static moment.

That is, $\bar{\boldsymbol{m}}_{s_1}$ (roll) depends linearly on δ_f and $\bar{\boldsymbol{m}}_{s_2}$ (yaw) is nearly independent of δ_f, that is, the effectiveness of δ_f is much smaller than that of C_μ, as seen in Fig. 6. The neglected effects of the flaperon deflection on $\boldsymbol{m}_s$ are regarded as part of $\boldsymbol{\delta m}_s$.

Note that the lack of dependency $\bar{\boldsymbol{m}}_{s_2}$ on δ_f will be shown to be convenient when inverting these characteristics to solve for C_μ and δ_f in subsequent sections because it eliminates the need for time-consuming iterations in the online control calculation.

IV. Control Design

A. System Description

The equations of motion describing the complete FTB system can be written in general terms as

$$\dot{\boldsymbol{x}} = f(\boldsymbol{x}) + g(\boldsymbol{x})\boldsymbol{m} \tag{24}$$

$$\dot{\boldsymbol{\eta}}_0 = \left(F_{a_0} + \delta F_a\right)\boldsymbol{\eta}_0 + \left(G_{a_0} + \delta G_a\right)[\bar{\boldsymbol{m}}_s(\boldsymbol{x}, \boldsymbol{u}) + \boldsymbol{\delta m}_s(\boldsymbol{x}, \boldsymbol{u})] \tag{25}$$

$$\boldsymbol{m} = H_{a_0}\boldsymbol{\eta}_0 \tag{26}$$

That is, it consists of a nonlinear system or plant [described by Eq. (24)] actuated by a subsystem comprising uncertain static nonlinearities and linear dynamics (25) and (26).

The measured output is

$$\boldsymbol{y} = [\boldsymbol{x}^T \quad \boldsymbol{m}^T]^T \tag{27}$$

where $\boldsymbol{x} \in R^{n_x}$, $\boldsymbol{\eta}_0 \in R^{n_\eta}$, $\boldsymbol{m}_s \in R^{n_m}$, $\boldsymbol{m} \in R^{n_m}$, $\boldsymbol{u} \in R^{n_u}$, $\boldsymbol{y} \in R^{n_x + n_m}$, and $n_\eta \geq n_m$. F_{a_0}, G_{a_0}, and H_{a_0} are known nominal constant matrices of appropriate size and δF_a and δG_a are uncertain matrices. Here $\bar{\boldsymbol{m}}_s(x, u)$ is the vector of known nominal nonlinearities, and $\boldsymbol{\delta m}_s(\boldsymbol{x}, \boldsymbol{u})$ is the vector of uncertain nonlinearities.

B. Assumptions

Several assumptions regarding the preceding set of equations are required or exploited in the derivations that follow. For clarity, these assumptions are stated here. These assumptions help define the class of nonlinear systems that will be addressed by the control design techniques developed.

For the main system, 1) $f(\boldsymbol{x})$ and $g(\boldsymbol{x})$ are known; 2) $g(\boldsymbol{x})$ is affinely bounded, that is, $\exists c_{g_i} \geq 0$, $i = 1, 2$, such that

$$\|g(\boldsymbol{x})\|_2 \leq c_{g_1}\|\boldsymbol{x}\|_2 + c_{g_2} \tag{28}$$

and 3) $\boldsymbol{x}$ is measurable.

For the subsystem, 1) all of the uncertainties can be collected into a lumped uncertainty $\boldsymbol{w} \in R^{n_m}$, which satisfies the matching condition,[12] that is,

$$G_{a_0}\boldsymbol{w} = \delta F_a\boldsymbol{\eta}_0 + G_{a_0}\boldsymbol{\delta m}_s(\boldsymbol{x}, \boldsymbol{u}) + \delta G_a\bar{\boldsymbol{m}}_s(\boldsymbol{x}, \boldsymbol{u}) + \delta G_a\boldsymbol{\delta m}_s(\boldsymbol{x}, \boldsymbol{u}) \tag{29}$$

$\forall \boldsymbol{x} \in R^{n_x}$, $\forall \boldsymbol{\eta}_0 \in R^{n_\eta}$, $\forall \boldsymbol{u} \in R^{n_u}$, $\forall \delta F_a$, $\forall \delta G_a$, and $\forall \boldsymbol{\delta m}_s(\boldsymbol{x}, \boldsymbol{u})$ given F_{a_0}, G_{a_0}, and $\bar{\boldsymbol{m}}_s(\boldsymbol{x}, \boldsymbol{u})$. Then, the subsystem (25) becomes

$$\dot{\boldsymbol{\eta}}_0 = F_{a_0}\boldsymbol{\eta}_0 + G_{a_0}[\bar{\boldsymbol{m}}_s(\boldsymbol{x}, \boldsymbol{u}) + \boldsymbol{w}] \tag{30}$$

2) Each component of the unknown w is not necessarily small but is bounded by an unknown constant, that is,

$$|w_i| \leq \rho_i(\text{unknown}), \qquad (i = 1, \ldots, n_m) \tag{31}$$

$\forall \boldsymbol{x} \in R^{n_x}$, $\forall \boldsymbol{u} \in R^{n_u}$ and $\forall \boldsymbol{\eta}_0 \in D$, where $D = \{\boldsymbol{\eta}_0 \in R^{n_\eta} \,|\, \|\boldsymbol{\eta}_0\|_2 < \infty\}$. 3) F_a, G_a, and H_a satisfy the following conditions: a) the triple (F_{a_0}, G_{a_0}, H_{a_0}) is minimal, b) G_{a_0} and H_{a_0} are full rank, c) $\det(H_{a_0}G_{a_0}) \neq 0$ (relative degree is one), d) invariant zeros of (F_{a_0}, G_{a_0}, H_{a_0}) are in the open left half-complex plane (minimum phase). The last assumption 4) $\boldsymbol{m}$ is measurable.

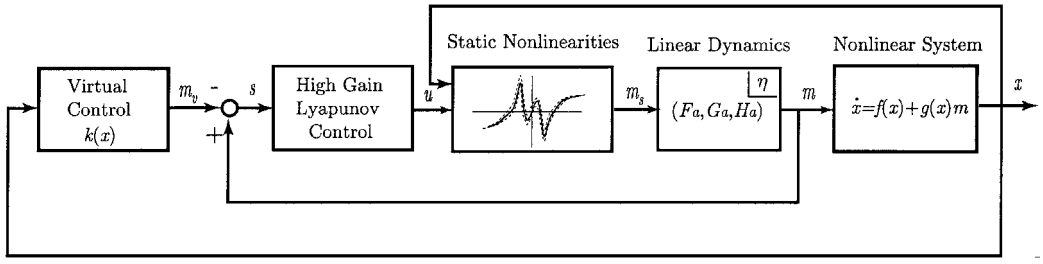

Fig. 8 Block diagram of controller/plant structure.

C. Nonlinear Control Design

Given an uncertain nonlinear system in the class just described, an approach to designing a nonlinear control is developed here that blends HGC[5,6] and Lyapunov techniques.[7,8,13,14] It can control the class of uncertain nonlinear systems in multiple timescales by robustly inverting the uncertain static nonlinearities.

Figure 8 shows the control structure incorporated. It consists of two control loops: an outer control loop (virtual control) and an inner control loop (high-gain Lyapunov control). The outer loop is designed assuming that the inner loop works perfectly ($\boldsymbol{m} = \boldsymbol{m}_v$ in Fig. 8). Then, the inner loop is designed to achieve robust, high-performance tracking of $\boldsymbol{m}_v$ by $\boldsymbol{m}$. Note that the inner-loop design depends explicitly on the outer-loop control design. The goal is to achieve performance of the entire closed-loop system that is close to that defined in the virtual control design step.

The details of the nonlinear control design process consist of three major steps: 1) virtual control (outer loop), 2) reduced-order observer, and 3) high-gain Lyapunov control.

1. *Step 1: Virtual Control*

The first step is to design a virtual control, or outer-loop design, that defines the desired overall system performance. That is, a continuous virtual controller $k(\boldsymbol{x})$ for the main system (24) is designed by ignoring the subsystem and regarding $\boldsymbol{m}$ as the control input. It is designed so that the closed-loop system

$$\dot{\boldsymbol{x}} = f(\boldsymbol{x}) + g(\boldsymbol{x})k(\boldsymbol{x}) \tag{32}$$

is stable and achieves desired performance. The design produced in this step typically yields a slower timescale closed-loop system than does the HGC inner-loop design.

2. *Step 2: Reduced-Order Observer*

The second step is to design a reduced-order observer to estimate any states in the subsystem that are not measured. This step is required because the last step of high-gain Lyapunov control requires an estimate of all of the states in the system. Note that if all subsystem states are measurable, this step is not required.

In particular, given the subsystem (30) and (26), an observer that achieves asymptotic decay of the state error in the presence of the lumped uncertainty w needs to be designed. The reduced-order observer approach[15] achieves asymptotic decay of the state error in the presence of the uncertainty without the information on the upper bounds of the uncertainty by transforming the system into a system where the uncertainty has no direct effect on the unmeasured states.

The following describes the design process of a reduced-order observer. The conditions on the triple (F_{a0}, G_{a0}, H_{a0}) ensure that it can be linearly transformed into the following form[16,17]:

$$F_a = \begin{bmatrix} F_{a11} & F_{a12} \\ F_{a21} & F_{a22} \end{bmatrix}, \qquad G_a = \begin{bmatrix} 0 \\ G_{a2} \end{bmatrix}, \qquad H_a = [0 \quad I] \tag{33}$$

The eigenvalues of F_{a11} are the stable invariant zeros of (F_{a0}, G_{a0}, H_{a0}) and $\boldsymbol{\eta}_0$ is transformed into

$$\boldsymbol{\eta}_0 \to \boldsymbol{\eta} = \begin{bmatrix} \boldsymbol{\eta}_1 \\ \boldsymbol{m} \end{bmatrix}$$

In the new coordinates, the subsystem dynamics are expressed as follows:

$$\dot{\boldsymbol{\eta}}_1 = F_{a11}\boldsymbol{\eta}_1 + F_{a12}\boldsymbol{m} \tag{34}$$

$$\dot{\boldsymbol{m}} = F_{a21}\boldsymbol{\eta}_1 + F_{a22}\boldsymbol{m} + G_{a2}[\bar{\boldsymbol{m}}_s(\boldsymbol{x}, \boldsymbol{u}) + \boldsymbol{w}] \tag{35}$$

The uncertainty $\boldsymbol{w}$ is isolated from the unmeasured states $\boldsymbol{\eta}_1$. It is assumed that the transformation from the original triple F_{a0}, G_{a0}, H_{a0} to the triple F_a, G_a, H_a in Eq. (33) has been applied in the subsequent sections.

From the transformed system, it is straightforward to design a reduced-order observer. A reduced-order observer for $\boldsymbol{\eta}_1$ in Eq. (34) is constructed as follows:

$$\dot{\hat{\boldsymbol{\eta}}}_1 = F_{a11}\hat{\boldsymbol{\eta}}_1 + F_{a12}\boldsymbol{m} \tag{36}$$

The error dynamics are

$$\dot{\tilde{\boldsymbol{\eta}}}_1 = F_{a11}\tilde{\boldsymbol{\eta}}_1 \tag{37}$$

Because F_{a11} is stable,

$$\tilde{\boldsymbol{\eta}}_1 \to 0 \quad \text{as} \quad t \to \infty \tag{38}$$

The estimate of $\boldsymbol{\eta}$ is

$$\hat{\boldsymbol{\eta}} = \begin{bmatrix} \hat{\boldsymbol{\eta}}_1 \\ \boldsymbol{m} \end{bmatrix}$$

The reduced-order observer yields state estimate $\hat{\boldsymbol{\eta}}$ such that

$$\hat{\boldsymbol{\eta}} = \boldsymbol{\eta} - \hat{\boldsymbol{\eta}} \to 0 (t \to \infty) \tag{39}$$

3. *Step 3: High-Gain Lyapunov Control*

The final step is to determine the actual control input u so that the $\boldsymbol{m}$ is close to the virtual control $k(\boldsymbol{x})$ designed in the first step.

A Lyapunov function approach is employed here to achieve small error between $\boldsymbol{m}$ and $k(\boldsymbol{x})$. The design process depends on the number of available inputs. In what follows, the number of inputs is equal to the dimension of $\boldsymbol{m}$, that is, $n_u = n_m$.

The inputs $\boldsymbol{u}$ are determined from the following vector control Lyapunov function $\boldsymbol{V}_s$ with $\boldsymbol{w} = 0$, $\boldsymbol{\eta} = \hat{\boldsymbol{\eta}}$:

$$\dot{\boldsymbol{V}}_s|_{w=0, \eta=\hat{\eta}} + 2\,\mathrm{diag}(\boldsymbol{\alpha}_s)\boldsymbol{V}_s = -\mathrm{diag}(\boldsymbol{\kappa})\boldsymbol{s}^2 \tag{40}$$

where a manifold $\boldsymbol{s}$ is defined as the difference between the virtual control $k(\boldsymbol{x})$ and the aerodynamic moments $\boldsymbol{m}$, that is,

$$\boldsymbol{s} = \boldsymbol{m} - k(\boldsymbol{x}) \tag{41}$$

and $\boldsymbol{V}_s$ is a vector control Lyapunov function for s:

$$\boldsymbol{V}_s = \begin{bmatrix} V_{s_1} & \cdots & V_{s_{n_m}} \end{bmatrix}^T = \begin{bmatrix} \frac{1}{2}s_1^2 & \cdots & \frac{1}{2}s_{n_m}^2 \end{bmatrix}^T \tag{42}$$

where $\boldsymbol{s}^2$ is $[s_1^2 \ \cdots \ s_{n_m}^2]^T$ and $\boldsymbol{\alpha}_s = [\alpha_{s_1} \ \cdots \ \alpha_{s_{n_m}}]^T$ is the desired decay rate of s. The decay rate is defined as the largest α_{s_i} such that

$$\lim_{t \to \infty} e^{\alpha_{s_i} t}|s_i(t)| = 0$$

holds for all trajectories of $s_i(t)$. This decay rate is selected faster than the timescale used in the virtual control design.

Note that $\boldsymbol{\kappa} = [\kappa_1 \ \cdots \ \kappa_{n_m}]^T$ is the vector of design parameters that determine the upper bound of $|s_i|, i = 1, \ldots, n_m$. The bound can be made small by increasing $\kappa_i, i = 1, \ldots, n_m$. However, increasing $\boldsymbol{\kappa}$ generally leads to larger control efforts. Equation (40) can be rewritten as

$$\text{diag}(\boldsymbol{s})\dot{\boldsymbol{s}}|_{w=0,\eta=\hat{\eta}} + \text{diag}(\boldsymbol{\alpha}_s)\boldsymbol{s}^2 = -\text{diag}(\boldsymbol{\kappa})\boldsymbol{s}^2 \tag{43}$$

Since

$$\dot{\boldsymbol{s}} = \dot{\boldsymbol{m}} - \dot{k}(\boldsymbol{x}) = H_a\{F_a\boldsymbol{\eta} + G_a[\bar{\boldsymbol{m}}_s(\boldsymbol{x}, \boldsymbol{u}) + \boldsymbol{w}]\} - \frac{\partial k(\boldsymbol{x})}{\partial \boldsymbol{x}}[f(\boldsymbol{x}) + g(\boldsymbol{x})\boldsymbol{m}] \tag{44}$$

$$\dot{\boldsymbol{s}}|_{w=0,\eta=\hat{\eta}} = H_a[F_a\hat{\boldsymbol{\eta}} + G_a\bar{\boldsymbol{m}}_s(\boldsymbol{x}, \boldsymbol{u})] - \frac{\partial k(\boldsymbol{x})}{\partial \boldsymbol{x}}[f(\boldsymbol{x}) + g(\boldsymbol{x})\boldsymbol{m}] \tag{45}$$

Eq. (43) becomes

$$\text{diag}(\boldsymbol{s})\left\{H_a[F_a\hat{\boldsymbol{\eta}} + G_a\bar{\boldsymbol{m}}_s(\boldsymbol{x}, \boldsymbol{u})] - \frac{\partial k(\boldsymbol{x})}{\partial \boldsymbol{x}}[f(\boldsymbol{x}) + g(\boldsymbol{x})\boldsymbol{m}]\right\} + \text{diag}(\boldsymbol{\alpha}_s)\boldsymbol{s}^2 = -\text{diag}(\boldsymbol{\kappa})\boldsymbol{s}^2 \tag{46}$$

Finally, the input $\boldsymbol{u}$ can be determined by solving the following equation [n_m equations for $n_u (= n_m)$ unknowns]. Note that $\boldsymbol{x}$, $\boldsymbol{m}$, and $\hat{\boldsymbol{\eta}}$ are known. Thus,

$$\bar{\boldsymbol{m}}_s(\boldsymbol{x}, \boldsymbol{u}) = \boldsymbol{m}_c(\boldsymbol{x}, \boldsymbol{m}, \hat{\boldsymbol{\eta}}) - (H_aG_a)^{-1}\text{diag}(\boldsymbol{\kappa})\boldsymbol{s} = \boldsymbol{m}_c(\boldsymbol{x}, \boldsymbol{m}, \hat{\boldsymbol{\eta}}) - \begin{bmatrix}\tilde{\kappa}_1 & \cdots & \tilde{\kappa}_{n_m}\end{bmatrix}^T\boldsymbol{s} \tag{47}$$

where $\boldsymbol{m}_c(\boldsymbol{x}, \boldsymbol{m}, \hat{\boldsymbol{\eta}})$ and $\tilde{\kappa}_i, i = 1, \ldots, n_m$, are defined as

$$\boldsymbol{m}_c(\boldsymbol{x}, \boldsymbol{m}, \hat{\boldsymbol{\eta}}) = -(H_aG_a)^{-1} \times \left\{H_aF_a\hat{\boldsymbol{\eta}} - \frac{\partial k(\boldsymbol{x})}{\partial \boldsymbol{x}}[f(\boldsymbol{x}) + g(\boldsymbol{x})\boldsymbol{m}] + \text{diag}(\boldsymbol{\alpha}_s)\boldsymbol{s}\right\} \tag{48}$$

$$\begin{bmatrix}\tilde{\kappa}_1 & \cdots & \tilde{\kappa}_{n_m}\end{bmatrix}^T = (H_aG_a)^{-1}\text{diag}(\boldsymbol{\kappa}) \tag{49}$$

The process of determining $\boldsymbol{u}$ from Eq. (47) requires an inversion of the static nonlinearities. Figure 9 shows an example of how to determine a single control input $\boldsymbol{u}$. In Fig. 9, the curve represents the nominal static nonlinearity $\bar{\boldsymbol{m}}_s(\boldsymbol{x}, \boldsymbol{u})$ given $\boldsymbol{x}$. The input $\boldsymbol{u}$ is determined from a point where the curve intersects the horizontal line at $[\boldsymbol{m}_c(\boldsymbol{x}, \boldsymbol{m}, \hat{\boldsymbol{\eta}}) - \tilde{\boldsymbol{\kappa}}^T\boldsymbol{s}]$, which is known at any instant because $\boldsymbol{x}$, $\boldsymbol{m}$, and $\hat{\boldsymbol{\eta}}$ are known. When multiple intersections exist, the minimum amount of the input will be chosen. Note that with the same $\boldsymbol{m}_c(\boldsymbol{x}, \boldsymbol{m}, \hat{\boldsymbol{\eta}})$, a different input results depending on the sign of $\tilde{\boldsymbol{\kappa}}^T\boldsymbol{s}$. In this way, the static nonlinearities are inverted to determine the inputs.

In general, solving Eq. (47) when there are multiple inputs, that is, u is not a scalar, can require an iterative scheme, and depending on the system, this could be problematic for real-time implementations. However, as will be shown, this was not an issue for the experimental system dealt with here because the solutions for the two control inputs C_μ and δ_f can be decoupled.

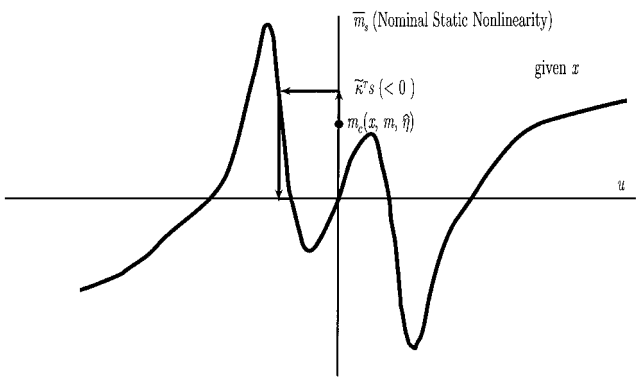

Fig. 9 Inversion of nonlinearity (determination of C_μ).

D. Discussion

The resulting controller/plant structure is shown in Fig. 8. The key element is that the inner loop achieves small error in the presence of the uncertainties. The inner-loop control (high-gain Lyapunov control) takes the effect of the uncertainties on the stability into account in a selective way. When the size of the uncertainties is large, the control renders the effective gain of the controller selectively high. The control can adjust the control input to counteract the large uncertainties. The selective adjustment is made possible with the measurement of $\boldsymbol{m}$ that contains information of the uncertainties. The main idea behind the selective adjustment of the control gain according to the size of uncertainties comes from the nonlinear damping technique.[8] Essentially, the nonlinear approach in this section is an application of the nonlinear damping technique to a smaller dimensional error space, the idea of which comes from sliding mode control.[14]

E. Proofs

To prove that the control design approach yields a feasible controller, several proofs are required. In particular, it must be shown that 1) $\tilde{\boldsymbol{\eta}}$ is bounded, 2) $\boldsymbol{u}$ resulting from Eq. (47) renders $\boldsymbol{s}(t)$ bounded for any $\boldsymbol{w}$, 3) $\boldsymbol{x}$ is bounded, and 4) $\boldsymbol{\eta}$ is bounded. These proofs are presented in the Appendix.

V. Application to FTB

The nonlinear control design approach presented is applied here to the FTB system. In particular, set-point tracking of the two-DOF system with FTB and flaperons is presented. This example serves to demonstrate the steps in the control design process and to show that the process can achieve effective control laws.

A. System Description

The main system equations are of the form

$$\dot{\boldsymbol{x}} = f(\boldsymbol{x}) + g(\boldsymbol{x})\boldsymbol{m} \tag{50}$$

with details defined in Eq. (10). The state is $\boldsymbol{x} = [\boldsymbol{q}^T \ \dot{\boldsymbol{q}}^T]^T = [\phi \ \gamma \ \dot{\phi} \ \dot{\gamma}]^T$.

The measured output vector of the FTB system is

$$\boldsymbol{y} = [\boldsymbol{q}^T \quad \dot{\boldsymbol{q}}^T \quad \ddot{\boldsymbol{q}}^T]^T = [\phi \quad \gamma \quad \dot{\phi} \quad \dot{\gamma} \quad \ddot{\phi} \quad \ddot{\gamma}]^T \tag{51}$$

The function $g(x)$ in Eq. (50) is norm bounded, that is,

$$\|g(\boldsymbol{x})\|_2 \le c_{g2} \tag{52}$$

because

$$g(\boldsymbol{x}) = \begin{bmatrix}0 \\ H(\boldsymbol{q})^{-1}\end{bmatrix} \tag{53}$$

from Eq. (10), and $H(\boldsymbol{q})$ satisfies[18]

$$\underline{\lambda}_{\min} I \le H(\boldsymbol{q}) \le \bar{\lambda}_{\max} I \tag{54}$$

for all possible $\boldsymbol{q}$. Therefore, c' in Eq. (A13) is always positive because $c_{g1} = 0$ in this case,

$$c' = c_3 - c_4c_{g1}c_s = c_3 > 0 \tag{55}$$

Hence, all of the conditions of the main system are satisfied.

The equations describing the subsystem were defined in Eqs. (15) and (16) as

$$\dot{\boldsymbol{m}} = F_a\boldsymbol{m} + G_a\boldsymbol{m}_s(\boldsymbol{x}, \boldsymbol{u}) \tag{56}$$

Here two independent first-order lags for both aerodynamic moments are considered; hence, all of the conditions on the triple F_{a0}, G_{a0}, H_{a0} are satisfied. Also, all of the uncertainty is assumed to be in $\boldsymbol{m}_s(\boldsymbol{x}, \boldsymbol{u})$ (which is represented by tables of experimental data).

Finally, $\boldsymbol{m}$ is measured because it can be computed from Eq. (9) using the angular accelerations $\ddot{\phi}$ and $\ddot{\gamma}$. Note, because noise in the

accelerations directly results in an error in computation of $\boldsymbol{m}$, both accelerations are filtered with analog prefilters. (The resulting error in $\boldsymbol{m}$ can be regarded as another source of uncertainties.)

Hence, all of the conditions of the subsystem are also satisfied.

B. Virtual Control

The outer-loop or virtual control design for the rigid-body system given by Eq. (50) can be accomplished in many different ways. Here, a simple proportional–integral–derivative (PID) control system was selected because it is easily calculated and because PID control for rigid-body dynamic systems gives semiglobally stabilizing control due to the passive nature of the rigid body.[19] Specifically, as noted in Sec. III.A, the rigid-body dynamics of the FTB system can be decomposed into two independent linear, time-invariant (LTI) systems; hence, a virtual control can be designed with simple pole assignment for each LTI system. The result is

$$[C_\mu \delta_f]^T = [K_p K_d K_i]\left[\boldsymbol{q}^T \dot{\boldsymbol{q}}^T \int \boldsymbol{q}^T \, \mathrm{d}t\right]^T \tag{57}$$

where

$$K_p = \begin{bmatrix} 0.0206 & 0 \\ 0 & 0.4164 \end{bmatrix}, \qquad K_i = \begin{bmatrix} 0.0419 & 0 \\ 0 & 0.4854 \end{bmatrix}$$

$$K_d = \begin{bmatrix} 0.0027 & 0 \\ 0 & 0.1364 \end{bmatrix}$$

C. Reduced-Order Observer Design

Because full state information is available in this case for the subsystem, that is, $\boldsymbol{\eta} = \boldsymbol{m}$ and $\boldsymbol{m}$ is measurable, a reduced-order observer (step 2) is not necessary.

D. High-Gain Lyapunov Control

For this step, the system and subsystem were defined by Eqs. (50) and (56). Here, x and $\boldsymbol{m}$ are measured quantities.

There are two sets of design parameters that characterize the performance of the HGC design. The first is the vector of desired decay rates $[\alpha_{s1} \;\; \alpha_{s2}]$ on the tracking errors defined by $s_i = \boldsymbol{m}_i - k(\boldsymbol{x})_i$. For this example, each of the decay rates of s_i, $i = 1, 2$, is set to 10 (which is about 10 times faster than the virtual closed loop for the rigid-body dynamics). That is,

$$\boldsymbol{\alpha}_s = [10 \quad 10]^T$$

The second parameter is $[\kappa_1 \;\; \kappa_2]$. This vector determines upper bounds on the tracking errors $|s_i|$. The results for several sets of $\boldsymbol{\kappa}$ are presented in the experimental results section to follow to show how $\boldsymbol{\kappa}$ can be used to trade closed-loop performance against control usage.

Having specified all design parameters, the HGC control is found at each time step by 1) computing $\tilde{\boldsymbol{\kappa}}$ from Eq. (49), 2) computing $\boldsymbol{m}_c$ from Eq. (48), and 3) solving the nonlinear Eq. (47) for $\boldsymbol{u} = [C_\mu \;\; \delta_f]$, where $\bar{\boldsymbol{m}}_s(\boldsymbol{x}, \boldsymbol{u})$ is given by Eqs. (22) and (23).

Note that because Eqs. (22) and (23) are one-way coupled in this case, an online implementation is straightforward. Equation (23) is solved for C_μ using the graphical technique discussed in Sec. IV.c.3, and Eq. (22) is then solved algebraically for δ_f.

E. Experimental Results

Two-DOF set-point tracking experiments were conducted at a 100-Hz sampling rate. The results are shown in Figs. 10 and 11. Figure 10 shows the data when $\boldsymbol{\kappa}$ is relatively small ($\boldsymbol{\kappa} = [40 \;\; 140]^T$). Figure 11 represents a case where $\boldsymbol{\kappa} = [400 \;\; 1400]^T$. At this level $\boldsymbol{\kappa}$, the control structure behaves like a conventional bang–bang control. In Fig. 10, it is seen that the set points ($\phi = 20$ deg, $\gamma = 10$ deg) are achieved with smaller air usage (the average $C_\mu = 0.01$ in $t \in [0 \;\; 5]$) than in Fig. 11 (the average $C_\mu = 0.029$ in $t \in [0 \;\; 5]$). Each component of s rapidly converges to within a small bound as shown in Fig. 10, whereas each component of $\boldsymbol{s}$ is contained in a small bound in Fig. 11. The bounds of both ϕ ($\Delta\phi = 5.1$ deg) and γ ($\Delta\gamma = 1.7$ deg) in the steady state in Fig. 10 are degraded compared to the result of the bang–bang control ($\Delta\phi = 2.5$ deg, $\Delta\gamma = 2.1$ deg). Also, note that the flaperons move very rapidly to cancel the roll moment generated by the small levels of blowing. The roll moment in the small levels of blowing is large and rapidly changing with C_μ. On the other hand, the flaperons in the bang–bang control do not move rapidly due to the benign roll moment characteristics in the large

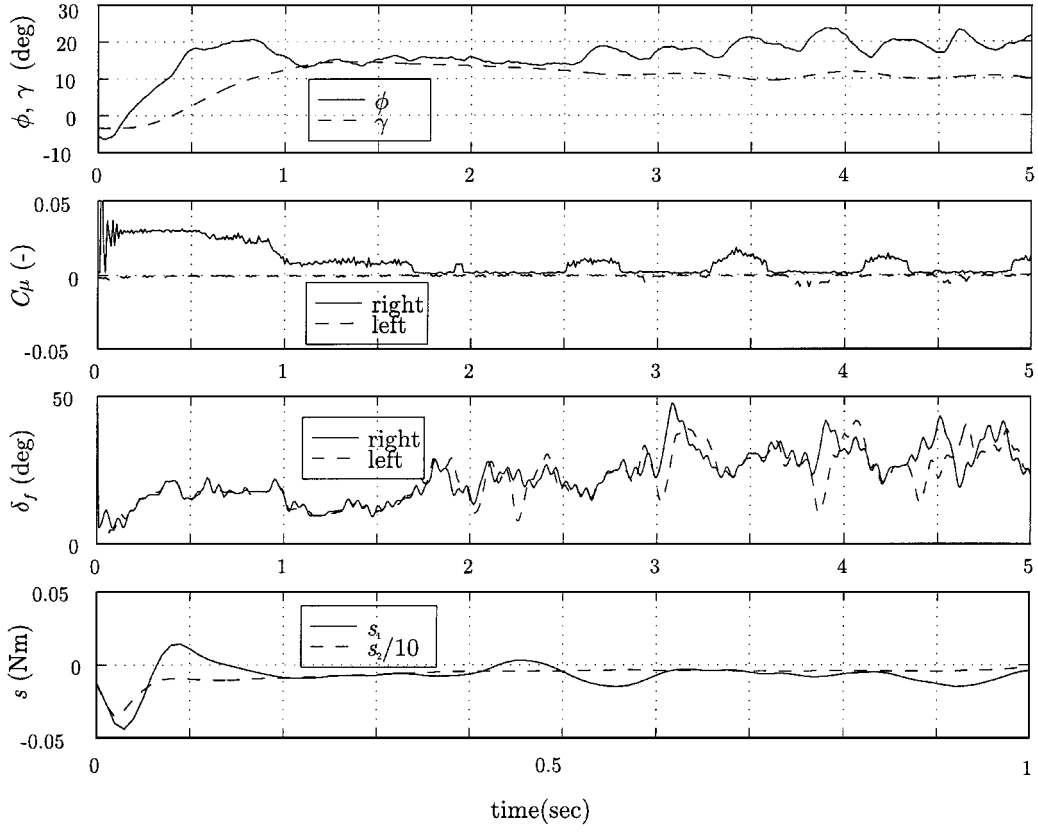

Fig. 10 Two-DOF set-point tracking (experiment), $\kappa = [40 \;\; 140]$.

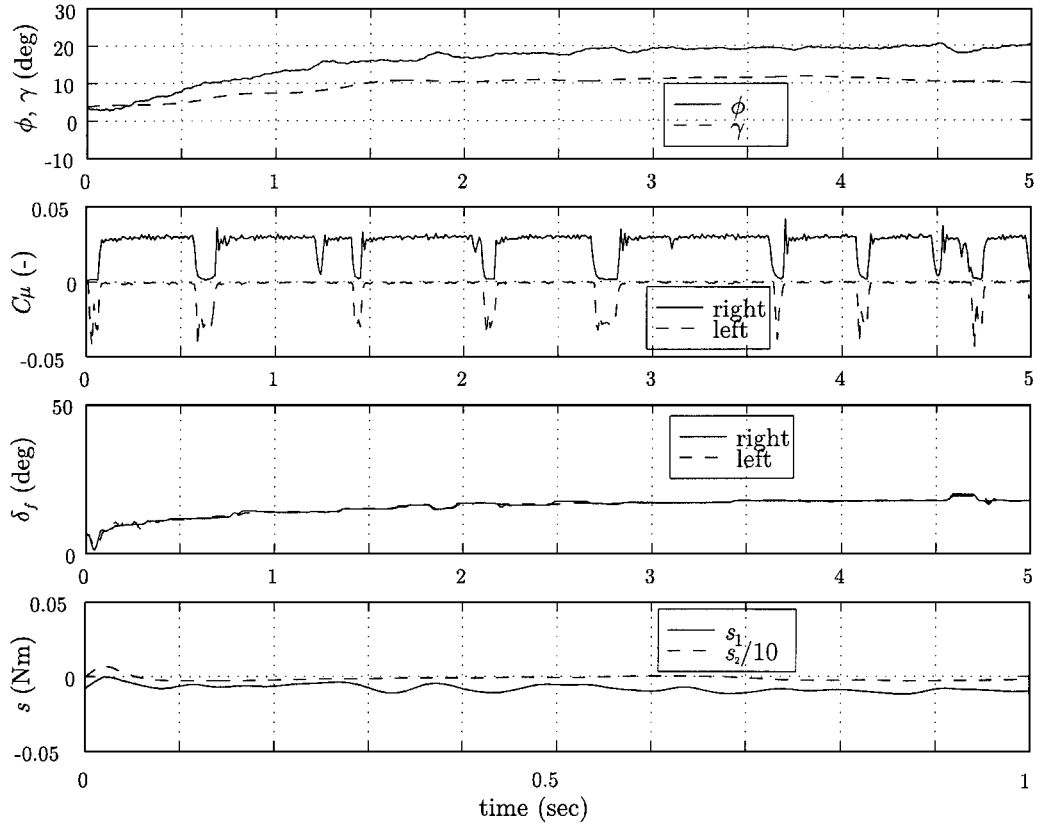

Fig. 11 Two-DOF set-point tracking (experiment), $\kappa = [400\ \ 1400]$ (bang–bang).

levels of blowing. When the two cases shown are compared, it is observed that, with the smaller $\boldsymbol{\kappa}$, the amount of air usage is reduced to about one-third, whereas the bound of the controlled output is increased by a factor of two.

VI. Conclusions

A nonlinear control approach has been developed that robustly inverts uncertain nonlinearities. It is applicable to nonlinear systems that are actuated by a subsystem comprising uncertain static nonlinearities and linear dynamics. The approach consists of three simple steps that allow timescale separation of each step. Neither upper bounds on the uncertainties nor a full dimensional Lyapunov function is required. It allows explicit trade-off between the performance and the control effort. The control design has been applied to FTB to exploit fully FTB efficiency. Independent set-point tracking control of roll and yaw angles at a high angle of attack with FTB and flaperons has been successfully demonstrated experimentally.

Appendix: Proofs

A. Boundedness of $\tilde{\eta}$

Since $\tilde{\eta}_1 \to 0$, and $\tilde{\boldsymbol{\eta}}$ is constructed as

$$\tilde{\boldsymbol{\eta}} = \begin{bmatrix} \tilde{\eta}_1 \\ 0 \end{bmatrix}$$

$\tilde{\boldsymbol{\eta}}$ is bounded,

$$\|\tilde{\boldsymbol{\eta}}\|_2 \le c_{\tilde{\eta}} \tag{A1}$$

where $c_{\tilde{\eta}}$ is the upper bound of $\tilde{\boldsymbol{\eta}}$.

B. Boundedness of s

With u determined from Eq. (47), the following inequality holds:

$$\begin{aligned}\dot{\boldsymbol{V}}_s + 2\mathrm{diag}(\boldsymbol{\alpha}_s)\boldsymbol{V}_s &= \dot{\boldsymbol{V}}_s|_{w=0,\eta=\dot{\eta}} + 2\,\mathrm{diag}(\boldsymbol{\alpha}_s)\boldsymbol{V}_s \\ &\quad + \mathrm{diag}(\boldsymbol{s})(H_a F_a \tilde{\boldsymbol{\eta}} + H_a G_a \boldsymbol{w}) \\ &= \mathrm{diag}(\boldsymbol{s})(H_a F_a \tilde{\boldsymbol{\eta}} + H_a G_a \boldsymbol{w}) - \mathrm{diag}(\boldsymbol{\kappa})\boldsymbol{s}^2 \\ &= \mathrm{diag}(\boldsymbol{s})\tilde{\boldsymbol{w}} - \mathrm{diag}(\boldsymbol{\kappa})\boldsymbol{s}^2 \preceq \mathrm{diag}(|\boldsymbol{s}|)\tilde{\boldsymbol{\rho}} - \mathrm{diag}(\boldsymbol{\kappa})\boldsymbol{s}^2 \end{aligned} \tag{A2}$$

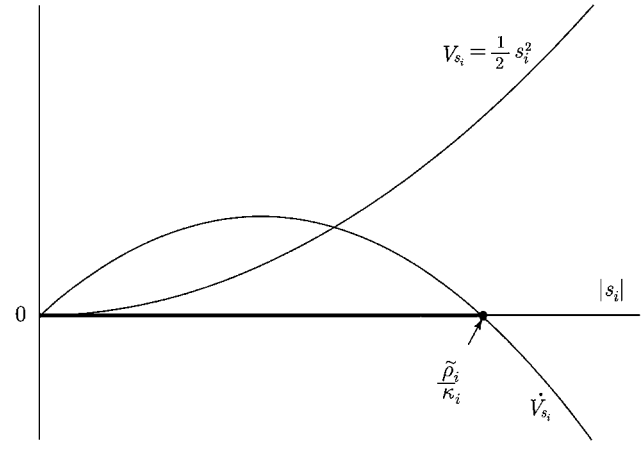

Fig. A1 Boundedness of s.

where $\tilde{\boldsymbol{w}} = H_a F_a \tilde{\boldsymbol{\eta}} + H_a G_a \boldsymbol{w}$ and $\tilde{\rho}_i = |\tilde{w}_i|$, $i = 1, \ldots, n_m$. Here $|\boldsymbol{s}|$ is defined as $[|s_1| \cdots |s_2|]^T$, and $\preceq$ represents componentwise inequality. Note that $\tilde{\rho}_i$, $i = 1, \ldots, n_m$, is unknown but bounded. The right-hand side of each component of Eq. (A2) reduces to

$$\begin{aligned} -\kappa_i s_i^2 + \tilde{\rho}_i |s_i| &= -\kappa_i |s_i| [|s_i| - (\tilde{\rho}_i/\kappa_i)] \\ &= -\kappa_i \left[|s_i| - (\tilde{\rho}_i/2\kappa_i)^2 + \tilde{\rho}_i^2 \big/ 4\kappa_i \right], \qquad (i = 1, \ldots, n_m) \end{aligned} \tag{A3}$$

In summary, it has been shown

$$\begin{aligned} V_{s_i} &= \tfrac{1}{2} s_i^2 \ge 0 \\ \dot{V}_{s_i} + 2\alpha_{s_i} V_{s_i} &\le -\kappa_i (|s_i| - \tilde{\rho}_i/2\kappa_i)^2 + \tilde{\rho}_i^2 \big/ 4\kappa_i \end{aligned} \tag{A4}$$

Figure A1 shows the situation when $\boldsymbol{\alpha}_s$ is zero. When $|s_i(t)|$ is larger than $\tilde{\rho}_i/\kappa_i$, $\dot{V}_{s_i}$ becomes negative. This implies that V_{s_i} is decreasing as a function of time. Therefore, $|s_i(t)|$ is also decreasing

because V_{s_i} is a radially unbounded positive definite function of $|s_i(t)|$. In this way, $|s_i(t)|$ is ultimately bounded above by $\tilde{\rho}_i/\kappa_i$. The bound can be made small by increasing κ_i, $i = 1, \ldots, n_m$, without knowing the upper bound of the uncertainties $\tilde{\rho}_i$. However, increasing κ normally leads to larger control efforts. Therefore, it is concluded that s_i, $i = 1, \ldots, n_m$, is ultimately bounded for any $\kappa_i > 0$, that is,

$$|s_i(t)| \le \tilde{\rho}_i/\kappa_i, \qquad (i = 1, \ldots, n_m) \tag{A5}$$

For all positive design parameter $\boldsymbol{\kappa}$, $\boldsymbol{s}$ is bounded, and $\boldsymbol{\kappa}$ determines the upper bound of $\boldsymbol{s}$. If the estimates of the bounds $\tilde{\boldsymbol{\rho}}$ of uncertainties are available, the upper bounds of s can be computed a priori from Eq. (A5). The information can be used to estimate the upper bound of the controlled variables (the worst-case performance). Therefore, κ can be computed a priori, given the requirement of the worst-case performance.

Note that $\tilde{\boldsymbol{\eta}}$ is not required to converge to 0, but merely to be bounded. Also note the 2-norm of s is bounded because each component of s is bounded,

$$\|\boldsymbol{s}\|_2 \le c_s(\boldsymbol{\kappa}) \tag{A6}$$

where $c_s(\boldsymbol{\kappa})$ is the upper bound of $\|\boldsymbol{s}\|_2$, which is a function of $\boldsymbol{\kappa}$.

C. Boundedness of x

Let V_x be a Lyapunov function for the rigid-body states x. Because the main system (24) closed with the virtual control $\boldsymbol{k}(\boldsymbol{x})$ is (for simplicity, exponentially) stable, the following inequalities hold from the converse Lyapunov theorem (see Ref. 12):

$$c_1\|\boldsymbol{x}\|_2^2 \le V_x(\boldsymbol{x}) \le c_2\|\boldsymbol{x}\|_2^2 \tag{A7}$$

$$\dot{V}_x(\boldsymbol{x}) = \frac{\partial V_x(\boldsymbol{x})}{\partial \boldsymbol{x}}[f(\boldsymbol{x}) + g(\boldsymbol{x})k(\boldsymbol{x})] \le -c_3\|\boldsymbol{x}\|_2^2 \tag{A8}$$

$$\left\| \frac{\partial V_x(\boldsymbol{x})}{\partial \boldsymbol{x}} \right\|_2 \le c_4\|\boldsymbol{x}\|_2 \tag{A9}$$

for some positive constants c_i, $i = 1, \ldots, 4$. With the use of the same Lyapunov function $V_x(\boldsymbol{x})$ for the system with actual $\boldsymbol{m}$ not with the virtual control $\boldsymbol{k}(\boldsymbol{x})$, $\dot{V}_x(\boldsymbol{x})$ is evaluated as follows:

$$\begin{aligned}\dot{V}_x(\boldsymbol{x}) &= \frac{\partial V_x}{\partial x}[f(\boldsymbol{x}) + g(\boldsymbol{x})\boldsymbol{m}] = \frac{\partial V_x}{\partial x}\{f(\boldsymbol{x}) + g(\boldsymbol{x})[k(\boldsymbol{x}) + \boldsymbol{s}]\} \\ &\le -c_3\|\boldsymbol{x}\|_2^2 + \frac{\partial V_x}{\partial x}g(\boldsymbol{x})\boldsymbol{s} \le -c_3\|\boldsymbol{x}\|_2^2 + c_4\|\boldsymbol{x}\|_2\|g(\boldsymbol{x})\|_2\|\boldsymbol{s}\|_2\end{aligned} \tag{A10}$$

From the assumptions, $g(\boldsymbol{x})$ is affinely bounded.

$$\|g(\boldsymbol{x})\|_2 \le c_{g_1}\|\boldsymbol{x}\|_2 + c_{g_2}, \qquad c_{g_i} \ge 0 \qquad (i = 1, 2) \tag{A11}$$

Therefore,

$$\begin{aligned}\dot{V}_x(\boldsymbol{x}) &\le -(c_3 - c_4c_{g1}c_s)\|\boldsymbol{x}\|_2^2 + c_4c_{g2}c_s\|\boldsymbol{x}\|_2 \\ &= -c'\left[\|\boldsymbol{x}\|_2 - (c_4c_{g2}c_s/2c')^2\right] + \left[(c_4c_{g2}c_s)^2/4c'\right]\end{aligned} \tag{A12}$$

where

$$c' = c_3 - c_4c_{g1}c_s \tag{A13}$$

From the preceding inequality, if we can show that $c' > 0$, it follows that $\boldsymbol{x}$ is also bounded. Also, $c' > 0$ is always true if $g(\boldsymbol{x})$ is norm bounded because $c_{g1} = 0$ in this case and $c' = c_3 > 0$. Note that the bound on $\boldsymbol{x}$ also can be made small by increasing $\boldsymbol{\kappa}$ because increased gain leads to smaller ultimate bound of s (c_s). Thus, it can be concluded that the bound on x is also controlled by $\boldsymbol{\kappa}$.

D. Boundedness of η

Because $\boldsymbol{s}$ and $\boldsymbol{x}$ are bounded and $\boldsymbol{k}(\boldsymbol{x})$ is continuous, $\boldsymbol{m}[= k(\boldsymbol{x}) + \boldsymbol{s}]$ is also bounded. Therefore, it can be concluded from Eq. (34) that $\boldsymbol{\eta}_1$ is bounded because F_{a11} is stable and $\boldsymbol{m}$ is bounded. Consequently, all of the internal states $\boldsymbol{\eta}$ of the aerodynamic system (F_a, G_a, H_a) are bounded.

Acknowledgment

This work is supported by Air Force Office of Scientific Research Grant F49620-96-1-0248.

References

[1]Celik, Z. Z., and Roberts, L., "Aircraft Control at High-Alpha by Tangential Blowing," AIAA Paper 92-0021, 1992.

[2]Celik, Z. Z., and Roberts, L., "Vortical Flow Control on a Wing–Body Combination Using Tangential Blowing," AIAA Paper 92-4430, 1992.

[3]Adams, R. J., Buffington, J. M., and Banda, S. S., "Active Vortex Flow Control for VISTA F-16 Envelope Expansion," *Proceedings of the Guidance, Navigation, and Control Conference*, AIAA, New York, 1994, pp. 1259–1269.

[4]Pedreiro, N., Rock, S. M., Celik, Z. Z., and Roberts, L., "Roll–Yaw Control at High Angle of Attack by Forebody Tangential Blowing," AIAA Paper 96-0773, 1996.

[5]Marino, R., "High-Gain Feedback in Non-Linear Control Systems," *International Journal of Control*, Vol. 42, No. 6, 1985, pp. 1369–1385.

[6]Young, K. D., Kokotovic, P. V., and Utkin, V. I., "A Singular Perturbation Analysis of High-Gain Feedback Systems," *IEEE Transactions on Automatic Control*, Vol. 22, No. 6, 1977, pp. 931–938.

[7]Gutman, S., "Uncertain Dynamical Systems—Lyapunov Min–Max Approach," *IEEE Transactions on Automatic Control*, Vol. 24, No. 1, 1979, pp. 437–443.

[8]Kanellakopoulos, I., Kokotovic, P. V., and Morse, A., "A Toolkit for Nonlinear Feedback Design," *Systems Control Letters*, Vol. 18, No. 2, 1992, pp. 83–92.

[9]Pedreiro, N., "Experiments in Aircraft Roll–Yaw Control Using Forebody Tangential Blowing," Ph.D. Dissertation, Dept. of Aeronautics and Astronautics, Stanford Univ., Stanford, CA, Nov. 1997.

[10]Takahara, Y., "Nonlinear Flight Control Using Forebody Tangential Blowing," Ph.D. Dissertation, Dept. of Aeronautics and Astronautics, Stanford Univ., Stanford, CA, June 1999.

[11]Pedreiro, N., Takahara, Y., and Rock, S. M., "Aileron Effectiveness at High Angles of Attack: Interaction with Forebody Blowing," AIAA Paper 98-4518, 1998.

[12]Khalil, H., *Nonlinear Systems*, 2nd ed., Prentice–Hall, Upper Saddle River, NJ, 1996, p. 578.

[13]Corless, M. J., and Leitmann, G., "Continuous State-Feedback Guaranteeing Uniform Ultimate Boundedness for Uncertain Dynamic Systems," *IEEE Transactions on Automatic Control*, Vol. 26, No. 5, 1981, pp. 1139–1144.

[14]Hung, J. C., and Gao, W., "Variable Structure Control of Nonlinear Systems: A New Approach," *IEEE Transactions on Industrial Electronics*, Vol. 40, No. 1, 1993, pp. 45–55.

[15]Zak, S. H., and Hui, S., "Output Feedback Variable Structure Controllers and State Estimators for Uncertain/Nonlinear Dynamic Systems," *IEE Proceedings-D*, Vol. 140, No. 1, 1993, pp. 41–50.

[16]Edwards, C., "Sliding Mode Schemes Using Output Information with Application to Heating Plant Problems," Ph.D. Dissertation, Dept. of Engineering, Univ. of Leicester, Leicester, England, U.K., Dec. 1995.

[17]Edwards, C., and Spurgeon, S. K., "On the Development of Discontinuous Observers," *International Journal of Control*, Vol. 59, No. 5, 1994, pp. 1211–1229.

[18]de Wit, C. C., and Siciliano, B., *Theory of Robot Control*, Springer-Verlag, Berlin, 1996, p. 61.

[19]Arimoto, S., and Miyazaki, F., "Stability and Robustness of PID Feedback Control for Robot Manipulators of Sensory Capability," *Proceeding of the 1st International Symposium of Robotics Research*, MIT Press, Cambridge, MA, 1984, pp. 783–799.